Effect of pretreatment on microstructural stability and mechanical property in a spray formed Al-Zn-Mg-Cu alloy

Zhiping Wang [a], Mingliang Wang [a], Yugang Li [a], Hongyu Xiao [a], Han Chen [a], Jiwei Geng [a,b,*], Xianfeng Li [a,b], Dong Chen [a,b,*], Haowei Wang [a]

[a] State Key Laboratory of Metal Matrix Composites, Shanghai Jiao Tong University, Shanghai 200240, China
[b] Anhui Provincial Engineering Research Center of Aluminium Matrix Composites, Huaibei 235000, China

HIGHLIGHTS

- A new two-step pretreatment was proposed for spray formed Al alloy.
- Microstructural stability of Al alloy is enhanced by the new treatment.
- The strength is significantly enhanced by the proposed approach.
- The improved microstructural stability is related to Al_3Zr particles.

GRAPHICAL ABSTRACT
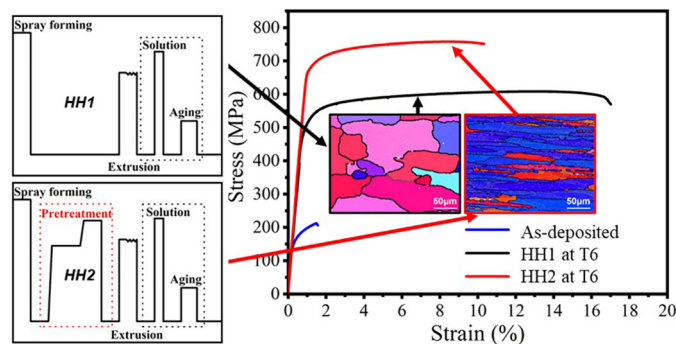
ARTICLE INFO

ABSTRACT

Aluminum alloys fabricated by spray forming (SF) technology are commonly followed by hot-working without heat treatments. A new approach that is a pretreatment before hot-working is proposed in the present work. The results show that the microstructural stability of materials processed by this new approach is improved evidently, which is related to the pinning effect on dislocations and grain boundaries by Al_3Zr particles induced during pretreatment. The strength of SF Al alloy processed by this treatment can be enhanced significantly. Owing to the combined effect of grain refinement strengthening, dislocation strengthening and precipitation strengthening, the yield strength and ultimate tensile strength can be enhanced by 171 MPa and 143 MPa, respectively. Based on experimental characterizations and a physical-based model, the underlying mechanisms regarding on enhancement of mechanical properties is mainly related to the induced Al_3Zr particles and the optimized precipitates by the pretreatment.

1. Introduction

Aluminum alloys are widely used for structure components in aerospace applications owing to a superior combination of high strength to density ratio, excellent mechanical properties, and fracture toughness [1–3]. Numerous methods are performed to enhance the strength and ductility by refining microstructure, reducing segregation or adjusting alloy composition, such as severe plastic deformation (e.g. equal channel angular pressing and high-pressure torsion), rapid solidification technology (e.g. additive manufacturing, powder metallurgy and spray forming (SF)). Among all these methods, SF can fabricate large-bulk billets by the successive deposition of atomized alloy as one of the rapid solidification technologies, which has the advantages of fine equiaxed grains, low segregation level and decreasing hot-cracks [4–6]. Thus, SF

* Corresponding authors at: State Key Laboratory of Metal Matrix Composites, Shanghai Jiao Tong University, Shanghai 200240, China.
E-mail addresses: gengjiwei163@sjtu.edu.cn (J. Geng), chend@sjtu.edu.cn (D. Chen).

has been recognized as an attractive and useful technology for developing high strength aluminum alloys.

Numerous studies of Al alloys produced by SF technology focused on forming mechanism of pores, alloy design, hot-deformation behavior and the following heat treatments. For instance, Cai et al. [7] gave an explanation of pores which formed in SF 2024 Al alloy and developed low-pressure SF technique. Sharma et al. [6] developed a high Mn composition alloy and showed high strength. Jia et al. [8] investigated the hot-deformation behavior of SF Al-Zn-Mg-Cu alloy and concluded that the deformation activation energy of SF alloy is relatively lower than that of the casting alloy owing to much finer microstructure, high solid solubility and reduced segregation at grain boundary (GB). Aging treatments make a great impact on microstructures, mechanical properties and corrosion behaviors of SF Al alloys by changing residual solid solution concentrations and distribution of GB precipitations, matrix phases and precipitate-free zones (PFZs) [9,10]. Also, the relationship between microstructure and mechanical property of SF Al alloys is reported frequently [11–17]. Generally, their works advanced the SF technology and demonstrated that the materials processed by SF showed good comprehensive mechanical property with homogenous microstructure. However, few works focused on the microstructural stability of SF Al alloys during heat treatments and the correlative effects on the mechanical properties.

Deformation (e.g. extrusion, rolling and forging) can further refine grains and optimize microstructures to enhance the strength. For the deformable and heat-treatable Al alloys, keeping the stability of grain structures during the following heat treatments is crucial for increasing mechanical properties of the components [18]. It is proved that additions of Zr in Al alloys can effectively improve their microstructural stability and properties by forming nano Al_3Zr particles [19]. The improved microstructural stability is attributed to the effects of particles on recrystallization and grain growth since they can effectively pin dislocations and GBs at elevated temperatures during hot deformation and solution treatments [20,21,22]. Moreover, the precipitation of Al_3Zr requires long-time annealing at high temperature due to slow diffusion rate of Zr element [23]. In ingot metallurgy (IM) alloy, homogenization treatment is often needed before deformation to reduce microsegregation and induce precipitation of the particles [24,25]. In SF Al alloys, homogenous microstructures with low segregation and fine grains were reported repeatedly [8,11,16,17,26,27]. The long-time annealing may break the refined microstructures [5,28]. Attributing to these facts, it is generally accepted that it should be better to deform directly from the SF Al alloy billets [5]. Thus, few works focused on the heat treatment for as-deposited billets. However, the precipitation of Al_3Zr particles should be strongly limited by conventional process (direct deformation after SF) of SF Al alloys with Zr addition, which can affect the microstructural evolution and mechanical properties. Recently, studies have reported the coarse grains of as-solutionized samples under conventional process [29,30]. Therefore, a pretreatment before hot deformation may be better for optimizing the microstructures of SF material by inducing the precipitation of dispersoids.

In this study, we aim to explore the microstructural stability and mechanical properties in the case of SF Al-Zn-Mg-Cu-Zr alloy. Before hot-extrusion, a pretreatment was added to improve the microstructural stability. The effect of pretreatment on the grain size and texture evolutions of SF Al-Zn-Mg-Cu-Zr alloy during heat treatment was investigated. Finally, the correlative strengthening mechanisms of the pretreated SF Al-Zn-Mg-Cu-Zr alloy were discussed.

2. Experimental details

2.1. Materials

The SF Al alloy billets were prepared in an environmental chamber. Before the SF process, the pure Al, Zn, Mg, Al–Cu and Al–Zr master alloys were fully melted to be atomized by nitrogen gas at 993–1073 K. The

distance of the atomizing deposition was kept constant at 650 mm. The typical round billets (Diameter, 360 mm; Height, 500 mm) were deposited for the experiment. The composition of as-deposited 7050 Al alloy is Al-6.52Zn-2.53 Mg-2.39Cu-0.12Zr (wt%).

2.2. Extrusion and heat treatments

There are two sets of heat treatments and deformation processes performing on the SF 7050 Al alloy billet in this work (Table 1). For the HH1 sample, the cylindrical specimens with a diameter of 40 mm were cut from SF billets and then directly extruded at 400 °C using an extrusion ratio of 16:1 with the extrusion speed of 0.8 mm/s. After hot extrusion, the diameter of extruded rod was 10 mm (as-extruded state). Afterwards, the as-extruded billet was solution treated at 477 °C for 60 min (477 °C@60 min) and quenched into water (as-solutionized state). Then, the aging treatment was performed at 120 °C for 24 h (120 °C@24 h) in order to achieve the peak aging (T6 state).

For the HH2 sample, the SF billet was cut into cylindrical specimens with a diameter of 40 mm and the specimens were heated by 300 °C@ 36 h and 470 °C@15 h with a heating rate of 100 °C/h from 300 °C to 470 °C, followed by quenching in water to avoid uncontrolled precipitation. This process is called as pretreatment and the benefit of this treatment should be discussed in the later part. Furthermore, the hot extrusion, solution and aging treatments were processed in the same manner with the HH1 sample.

2.3. Microstructural characterizations and tensile tests

The polarized light metallography was used to observe grain morphologies. The samples were polished and anodic coated by (3vol.% HBF_4 + 97vol.%H_2O) at 25 V. The X-ray diffraction (XRD) analyses were performed using a D8 ADVANCE DAVINCI X-ray diffractometer with Cu K_α radiation and the scan speed was 2°/min. ==Microstructures were examined by scanning electron microscopy (SEM, TESCAN MIRA3) equipped with energy dispersive spectroscopy (EDS).== Electron backscattered diffraction (EBSD) was conducted on the SEM to characterize the grains and grain boundaries (GBs). The step-size and accelerating voltage were 0.3 μm and 20 kV, respectively. The EBSD date was analyzed using the commercial software HKL CHANNEL 5. The GBs with the misorientation angles larger than 15° were defined as high angle grain boundaries (HAGBs, black lines), while those in 2°–15° were defined as low angle grain boundaries (LAGBs, gray lines) in the EBSD maps. The GBs with misorientation angles lower than 2° were not studied. The samples for transmission electron microscopy were prepared from 80 μm to 100 μm thick foils using a twin-jet electro-polishing system, and a (30% nitric acid +70% methanol) solution cooled to −30 °C and operated at 20 V. The TEM analyses were operated in the JEOL 2100F and Talos F200X at 200 kV. The mean radius, number density and volume fraction of the precipitates were quantified by image analysis of digitized TEM images. More than 200 particles were measured for each sample. The round specimens were used for tensile test, the gauge length five times the diameter. The tensile testing was carried out on a Zwick/Roell machine at a strain rate of 10^{-4} s^{-1} at room temperature according to ASTM E8/E8M-15a [31].

Table 1
Heat treatments and deformation processes of SF 7050 Al alloy billets.

Name	Pretreatment	Extrusion	Solution treatment	Aging treatment
HH1 sample	–	400 °C	477 °C@60 min	120 °C@24 h
HH2 sample	300 °C@36 h + 470 °C@15 h			

3. Results

3.1. Microstructure evolution during pretreatment

Fig.1 exhibits the backscattered electron (BSE) micrographs of both HH1 (Fig. 1a–b) and HH2 (Fig. 1c–d) samples before hot extrusion. For the HH1 sample, the fine equiaxed grains with the average size (d_{av}) of ~36 μm (Fig. 1a), which is distinguished from the dendrite structures of the reported as-cast 7050 alloy ($d_{av} = $ ~100 μm) [32]. The fine equiaxed grains of the HH1 sample are mainly due to two aspects [5,31]: (1) higher solidification rate during the flight process between atomizer and substrate; (2) hitting interaction between the sprayed droplets and top semi-solid layer.

Fig. 1b shows two types of secondary phases with distinct origins. The first type is the coarse phases formed at GBs during the solidification process caused by the segregation of alloying elements [12]. Quantitative metallographic analysis indicates a value ~2% in area for this type of segregation, which is a very low value in comparison with the conventional as-cast 7050 Al alloy (~7%) [33]. Thus, the element segregation of SF billet is less severe than the as-cast 7050 Al alloy. The second type is formed inside grains during the billet cooling. The XRD result (Fig. 1e) confirms that secondary phases should be $MgZn_2$ phases, and the corresponding element mapping images present both two types of secondary phases containing Mg, Zn, Cu elements. Thus, secondary phases can be regarded as $Mg(Zn,Cu,Al)_2$ due to Cu solutes dissolved into $MgZn_2$ phases [34]. Besides, few pores are observed, which are commonly formed in SF metals due to shrinkage for rapid cooling rate and suction for cooling gas [7].

For HH2 sample (Fig. 1c), many secondary phases are dissolved into the matrix after the pretreatment. A few undissolved intermetallics rich in Cu, Mg and/or Cu, Fe elements are observed (Fig. 1d), which are hard to be dissolved at the pretreatment temperature and frequently found in Al-Zn-Cu-Mg alloys [11].

3.2. Microstructure evolution during solution treatment

Fig. 2a and b exhibit the SEM micrographs of both as-extruded HH1 and HH2 samples, respectively. In both samples, most pores are
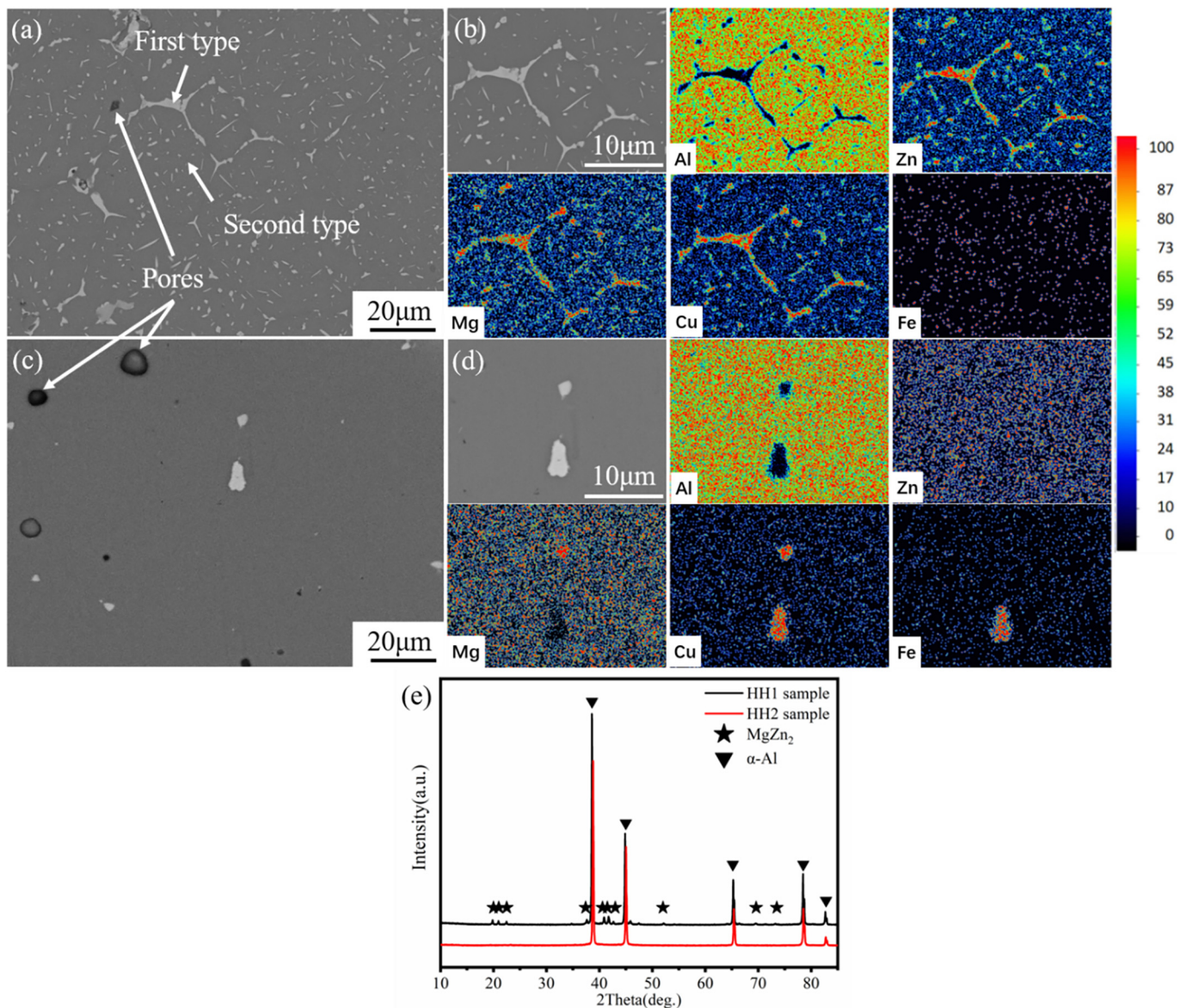

Fig. 1. Microstructures of samples before hot extrusion: (a) BSE micrograph of HH1, (b) enlarged area in (a) and corresponding element mappings; (c) BSE micrograph of HH2, (d) enlarged area at higher magnification in (c) and corresponding element mappings; (e) XRD results of HH1 and HH2.

eliminated by the hot extrusion, which is efficient to reduce the porosity of billet [13]. For HH1 sample (Fig. 2a), the secondary phases either formed inside grains or at GBs are aligned along the extrusion direction (ED) and some coarse phases are broken into fragments. The corresponding EDS results are listed in Table 2, and the secondary phases can be identified as Mg(Zn,Cu,Al)$_2$. This result is agreed with the microstructure of HH1 sample before hot extrusion (Fig. 1b and e). It suggests that these phases are generated during spray forming process. For HH2 sample (Fig. 2b), a number of coarse phases are aligned along ED. The number of coarse phases in the as-extruded HH2 sample is much less the HH1 sample and only few S(Al$_2$CuMg) phases can be found. Besides, a number of small precipitates can generate during hot extrusion in HH2 sample.

Fig. 2c and d display the EBSD maps of the as-extruded HH1 and HH2 sample, respectively. Both HH1 and HH2 sample show the typical ⟨001⟩ and ⟨111⟩ fiber textures along ED, in accordance with the results of extruded Al alloys [14,30]. The recrystallized fraction of as-extruded HH1 and as-extruded HH2 samples is 11.4% and 4.6%. It suggests that

Table 2
Chemical compositions (at.%) of the secondary phases in as-extruded samples.

Sample	Element	Al	Zn	Mg	Cu	Fe	Zr
HH1	A	58.37	18.09	14.88	8.61		0.01
	B	45.07	21.80	21.62	11.02	0.01	
HH2	C	50.24	2.22	23.84	23.65	–	0.01
	D	65.49	1.88	15.57	16.92	0.09	–

dynamic recrystallization occurs during hot extrusion in both as-extruded samples. After solution treatment, the recrystallized fraction of as-solutionized HH1 (Fig. 2e) and HH2 (Fig. 2f) samples is 95.1% and 12.4%. For the HH1 sample (Fig. 2e), it is found that the fiber textures have disappeared after solution treatment. The static recrystallization occurs in HH1 sample during solution treatment and the grains become more equiaxial with larger size. However, for the as-solutionized HH2 sample (Fig. 2f), the <001> and <111> fiber textures are still clearly observed. Both the grain morphologies and orientations
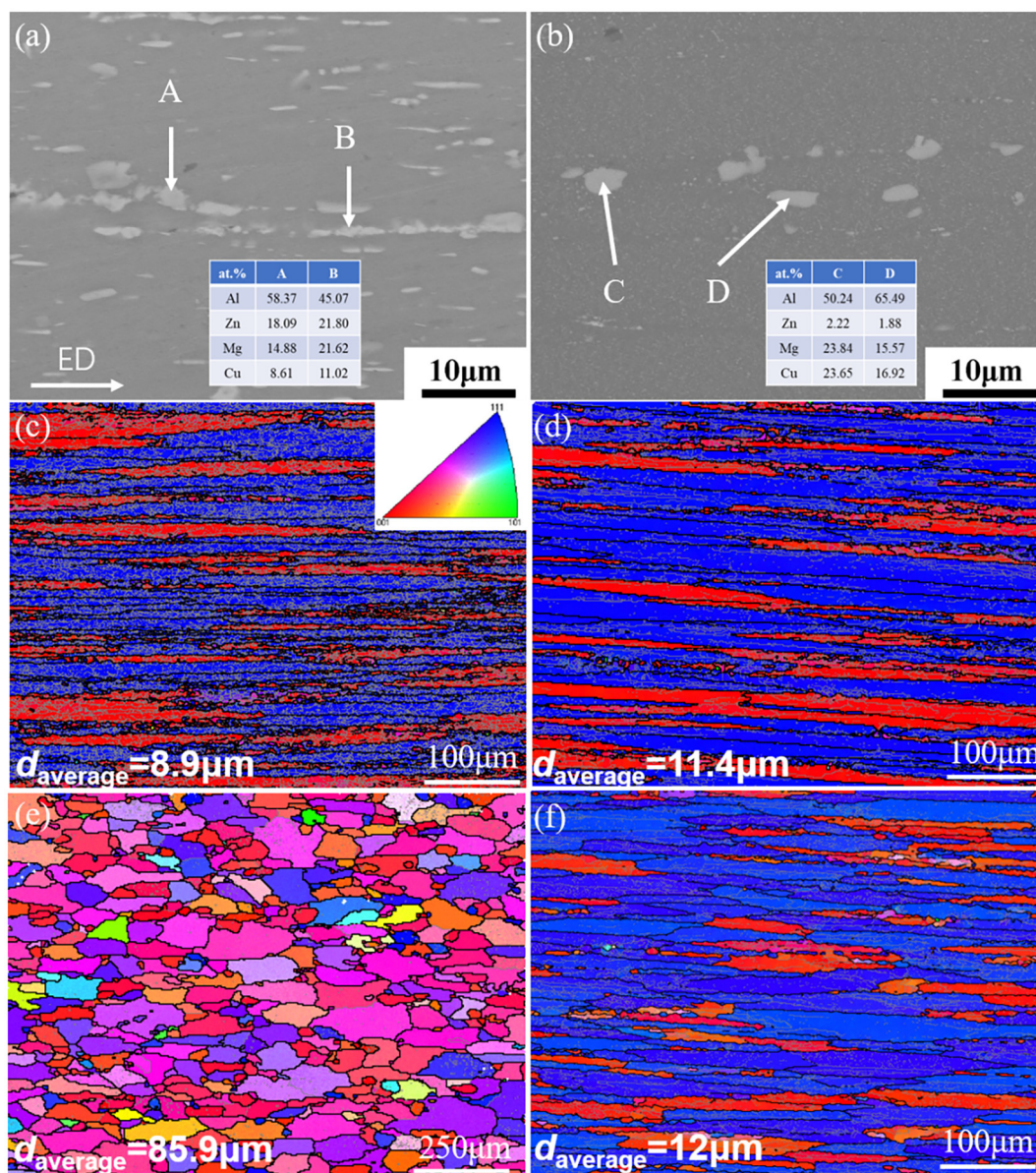
Fig. 2. BSE micrograph of as-extruded (a) HH1 and (b) HH2 sample, EBSD maps with IPF color coding of as-extruded (c) HH1 and (d) HH2 sample; EBSD maps of as-solutionized (477 °C@ 60 min) (e) HH1 and (f) HH2 sample.

of as-solutionized HH2 sample exhibit almost the same features with the as-extruded one. It indicates that the static recrystallization behavior of HH2 sample should be strongly impeded during solution treatment (477 °C@60 min).

Fig. 3 exhibits the grain size distribution and aspect ratio of two samples. For the as-extruded HH1 sample (Fig. 3a), the average grain size (d_{av}) is ~8.9 μm and the average grain aspect ratio (A_{av}) is ~4.0. After solution treatment, d_{av} is ~85.9 μm and A_{av} is ~2.5. Clearly, the value of d_{av} is increased by ~865% and the value of A_{av} is decreased by ~37.5%. For the as-extruded HH2 sample (Fig. 3b), d_{av} is ~11.4 μm and A_{av} is ~4.0. After solution treatment, d_{av} is ~12.0 μm and A_{av} is ~3.9. Notably, both the grain size and aspect ratio of HH2 sample are not obviously changed after 477 °C@60 min, showing excellent microstructural stability.

Comparatively, two as-extruded samples show little difference in the average grain size and grain aspect ratio. Importantly, the change of d_{av} and A_{av} suggest that not only static recrystallization but also grain growth occur in HH1 sample during solution treatment. In short, the microstructures of HH2 sample present much better stability in comparison with the HH1 sample during solution treatment.

3.3. Microstructure of both HH1 and HH2 samples after aging treatment

Fig.4 displays the cross-sectional EBSD maps of the extrusion rods. The d_{av} of HH1-T6 and HH2-T6 sample in the cross-sections is 37.4 μm and 6.3 μm, respectively. Besides, the insets are the corresponding maps of Taylor factor analyzed by CHANNEL 5. The average Taylor factor (M) of HH1-T6 and HH2-T6 samples are 2.901 and 3.252, respectively.

The variations of dislocations densities for both two samples are measured by XRD patterns (Fig. 5). The full-width at half-maximum (FWHM) of the peaks is obtained by deducting the instrumental broadening. There are mainly two reasons for the narrowing of Al peaks in the alloys [35], which are grain refinement and dislocations multiplication or annihilation. Therefore, the variations of the FWHM mainly demonstrate the change of dislocation densities. Dislocation densities can be estimated from peak broadening using the Williamson-Hall method [36]:

$$B\cos\theta = 2\varepsilon\sin\theta + \frac{\lambda}{d} \tag{1a}$$

$$\rho = \frac{\varepsilon\sqrt{3}}{db\sin\theta} \tag{1b}$$

where ρ is dislocation density, b is Burgers vector, d is average grain size, B is the FWHM of diffraction peak, λ is the wavelength of Cu K$_\alpha$ radiation (1.54 Å), θ is the Bragg angle. The dislocation density measured in the HH1-T6 sample is 8.3×10^{12} m^{-2}, while it is 7.5×10^{13} m^{-2} in the HH2-T6 sample. The HH2-T6 sample has much higher dislocation density than the HH1-T6 sample.

Fig. 6 exhibits the bright-field (BF) TEM images of HH1-T6 sample and HH2-T6 sample. Obviously, the equilibrium phase η (MgZn$_2$) and the matrix precipitates could be visualized directly on the TEM images. The η phases are distributed selectively on the GBs (Fig. 6a-b), where the nucleus for pre-precipitations is served under aging treatment. Fine and uniform precipitates are distributed within the grain under T6 treatment (Fig. 6c-d). And the width of PFZs of two samples is different. The
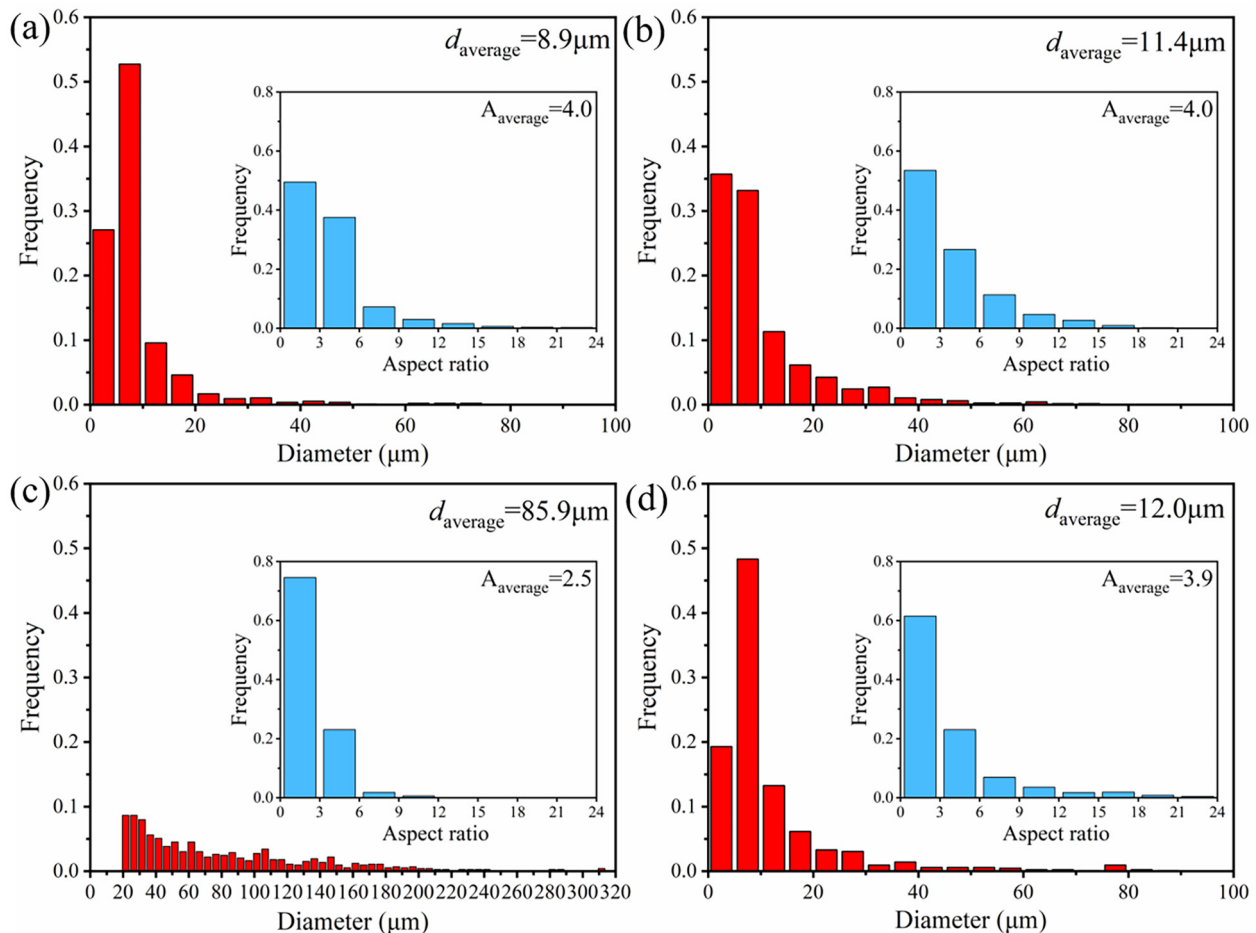

Fig. 3. Grain size distribution and grain aspect ratio under different conditions: (a) as-extruded HH1 sample, (b) as-extruded HH2 sample, (c) as-solutionized HH1 sample (477 °C@ 60 min), (d) as-solutionized HH2 sample (477 °C@60 min).
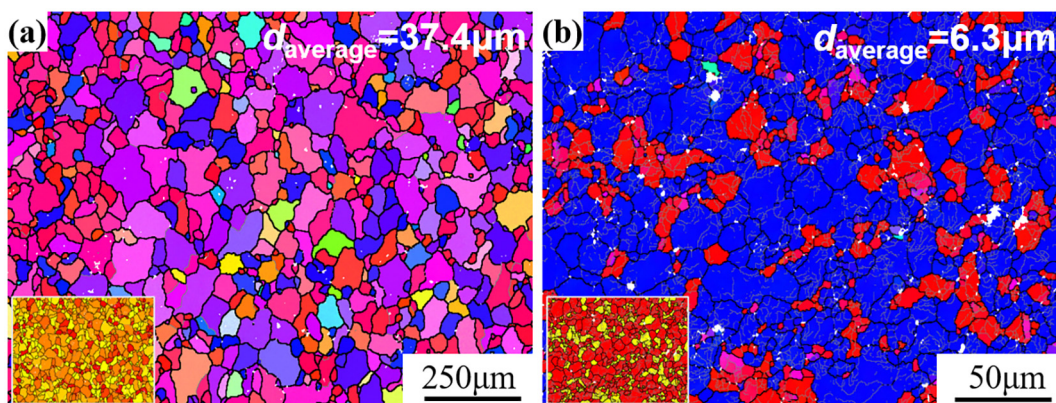
Fig. 4. Cross-sectional EBSD maps of extrusion rods: (a) HH1-T6, (b) HH2-T6. The insets are corresponding maps of Taylor factor analyzed by CHANNEL5.
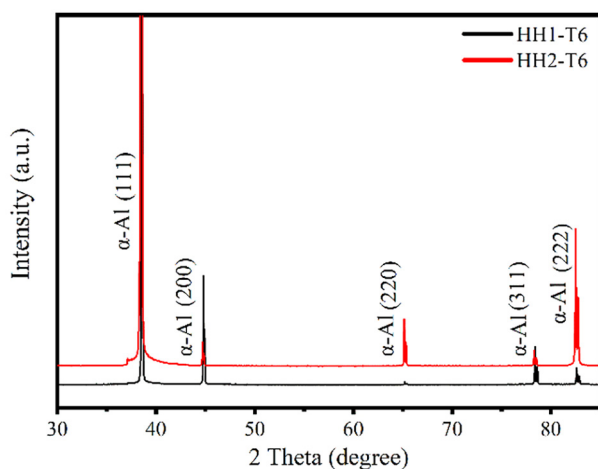

Fig. 5. XRD patterns of the SF 7050 Al alloys after aging treatment, the broadening peaks suggesting the higher dislocation density in HH2-T6 sample.

width of PFZ is ~25.2 nm for HH1-T6 sample, while no obvious PFZ is observed in HH2-T6 sample. Fig. 6e displays the high-resolution transmission electron micrograph (HRTEM) image of HH2-T6 sample which is obtained along the $[110]_{Al}$ zone axis in Al matrix. The FFT diffractogram (Fig. 6f) is consistent with the simulated diffractograms derived from the orientation relationships of η' precipitates with respect to the Al matrix: $(0001)_{\eta'}//(1\bar{1}1)Al$, $\left[10\bar{1}0\right]_{\eta'}//[110]Al$. This result is in agreement with Chung's work [37]. Besides, plate-like GPII zone (3–5 nm) is also observed in HRTEM and the zone forms on the $\{111\}_{Al}$ habit plane. Fig. 6g shows the precipitate size distribution for the aged alloys. The mean diameters of precipitates (including GPII zones and η' phases) are 5.3 nm and 4.8 nm for HH1-T6 and HH2-T6 sample. The precipitate size in HH2-T6 sample is smaller than the HH1-T6 sample.

3.4. Mechanical properties of both HH1 and HH2 samples

Table 3 shows the mechanical properties of the SF 7050 Al alloys and Fig. 7a shows the engineering stress-strain curves of HH1 and HH2 samples. Notably, pretreatment can effectively improve the yield strength (YS) and ultimate tensile strength (UTS) of the studied SF alloys. In as-solutionized samples, the YS and UTS are enhanced by ~90 MPa and ~114 MPa, respectively. Similarly, after aging treatment (120 °C@ 24 h), the YS and UTS of HH2 sample are also higher than those of HH1 sample. It proves that the pretreatment enhances the YS and UTS by ~171 MPa and ~143 MPa for T6 samples, respectively. Fig. 7b presents

the summaries of tensile properties of reported Al-Zn-Mg-Cu alloys after aging treatments [10,12,13,16,38–50]. Apparently, the strength of the SF 7050 Al alloy with pretreatment (HH2 sample) in our work is much higher than the alloy without pretreatment (HH1 sample) and reported Al-Zn-Mg-Cu alloys.

4. Discussion

Unlike the previous studies of SF Al alloys, a pretreatment of SF 7050 Al alloy was performed before hot extrusion in this study. The experimental results have shown that the proposed pretreatment can greatly prevent grain growth of SF 7050 Al alloy (HH2) in comparison with conventional SF process (HH1 sample), and hence the strength is significantly enhanced. The dominant mechanisms of microstructural stability and the correlative strengthening mechanism are discussed as follows.

4.1. Effect of pretreatment on microstructural stability

Fig. 8 shows the microstructure evolution of both HH1 and HH2 samples after different solution treatment time. For the HH1 sample (Fig. 8a–c), the grain size has increased dramatically after 477 °C@ 6 min due to recrystallization (Fig. 8b). With duration time increasing, the grain growth is not clearly observed (Fig. 8c). It suggests that the grain growth has dramatically occurred within 6 min and then grain size becomes relatively stable. Furthermore, the static recrystallization has occurred in less than 6 min. However, for the HH2 sample (Fig. 8d–f), the grain growth is not clearly found when the solution treatment time is increased from 6 min to 60 min. It exhibits the similar microstructures with the as-extruded state. The excellent microstructural stability of the HH2 sample should be attributed to the pretreatment before extrusion.

Microstructure evolutions at elevated temperature during solution treatment are closely related to the mobility of GBs and dislocations. In Fig. 9a, TEM image shows a great number of dislocations in as-extruded HH1 sample because of the plastic deformation by extrusion. After annealing at 477 °C@6 min (Fig. 9b), dislocations are significantly reduced. After annealing at 477 °C@60 min (Fig. 9c), few dislocations can be observed. Apparently, it is suggested that the dislocation rearrangement and annihilation have occurred in HH1 sample during solution treatment. However, the higher density of dislocations is found after solution treatments (Fig. 9d-h). In addition, a great number of η ($MgZn_2$) precipitates in as-extruded HH2 sample are confirmed by EDS analyses in STEM model (Fig. 9g and h), which are also detected by SEM (Fig. 2b, Fig. 9d). The coarse precipitates can pin dislocations during extrusion (Fig. 9g), leading to the increase in dislocations in the as-extruded HH2 sample. After annealing at 477 °C@6 min (Fig. 9e),
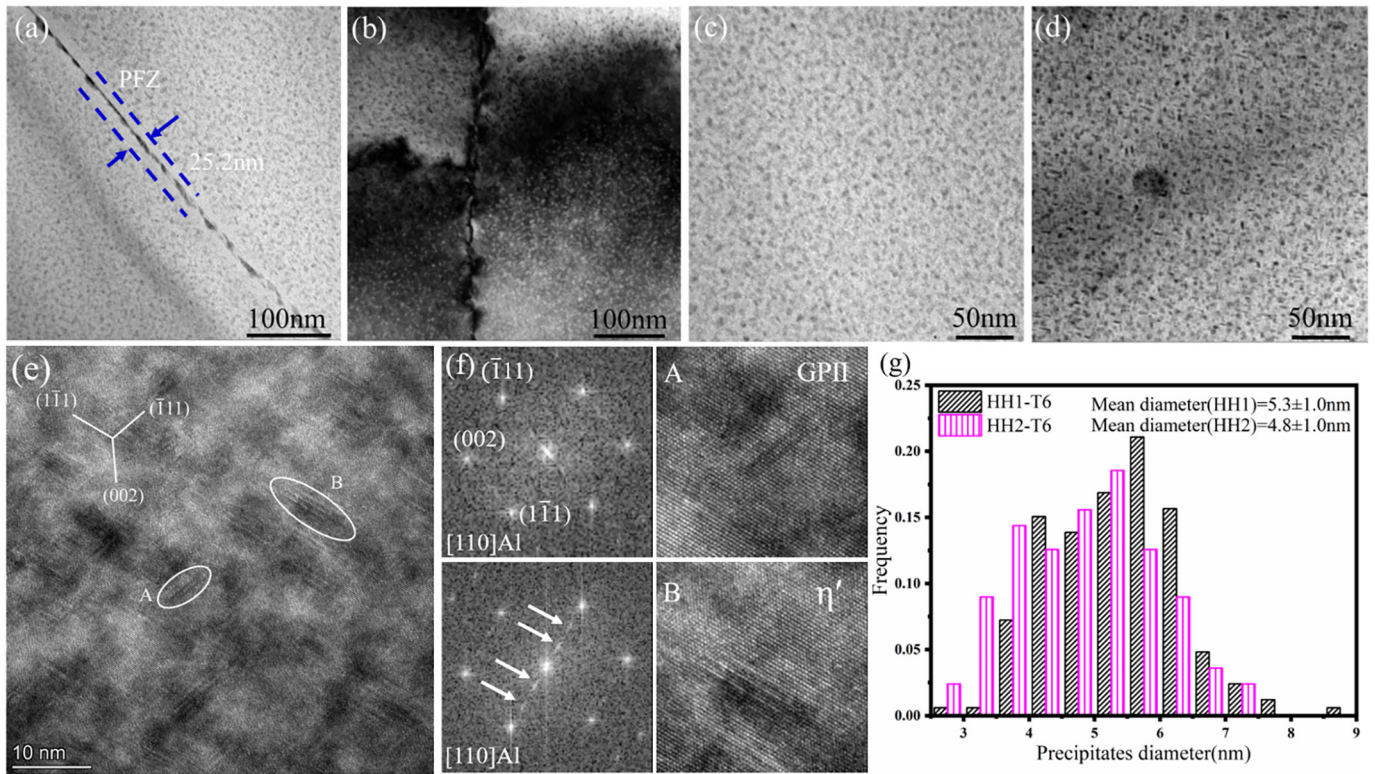
Fig. 6. TEM images showing the morphology of precipitates in 7050-T6 alloys: bright-field (BF) images of (a) HH1 and (b) HH2 sample, showing PFZ at GB; BF images showing uniformly distributed precipitates in (c) HH1 and (d) HH2 sample; (e) HRTEM image and (f) corresponding FFT and IFFT patterns, the orientation relationships of η' precipitates with respect to the Al matrix can be illustrated as follows: $(0001)_{\eta'}//(1\bar{1}1)$Al and $[10\bar{1}0]_{\eta'}//[110]$Al; (g) precipitate size distribution of two samples.

Table 3

Mechanical properties of SF 7050 Al alloys under different states (YS, yield strength; UTS, ultimate tensile strength).

Samples	YS (MPa)	UTS (MPa)	Elongation (%)
As-deposited	–	210 ± 4	1.5 ± 0.4
As-solutionized HH1	263 ± 4	474 ± 5	33 ± 2.2
As-solutionized HH2	353 ± 6	588 ± 2	12 ± 1.0
HH1-T6	512 ± 6	602 ± 5	16 ± 2.1
HH2-T6	683 ± 5	745 ± 8	10 ± 1.9

most of the precipitates have been dissolved into matrix, the dislocations are reduced. It suggests that η phases have no great contribution to the improvement of stability of dislocation since they are dissolved rapidly. After annealing at 477 °C@60 min (Fig. 9f), a large number of dislocations are pinned by small spherical particles, showing the improved stability of dislocations in comparison with HH1 sample.

In Fig. 10, the small spherical particles can be identified as Al$_3$Zr particles, whose L1$_2$ structure is ascertained by the selected area electron diffraction (SAED) pattern and HRTEM image. The Al$_3$Zr particles are
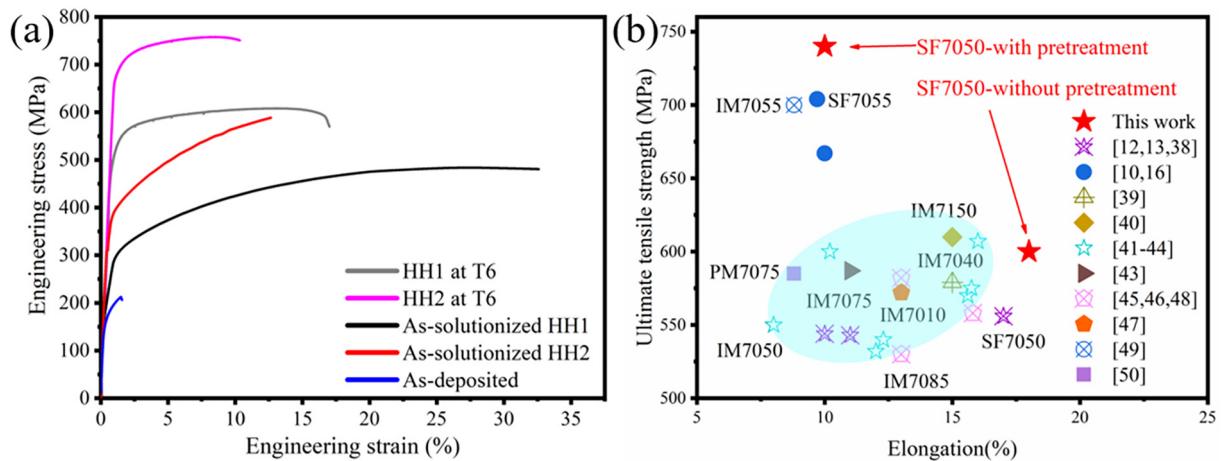
Fig. 7. (a) Engineering stress-strain curves of HH1 and HH2 sample at different states, (b) comparison of tensile properties of this studied SF 7050 Al alloy with the reported Al-Zn-Mg-Cu alloys. (IM: Ingot metallurgy; PM: Powder metallurgy; SF: Spray forming).
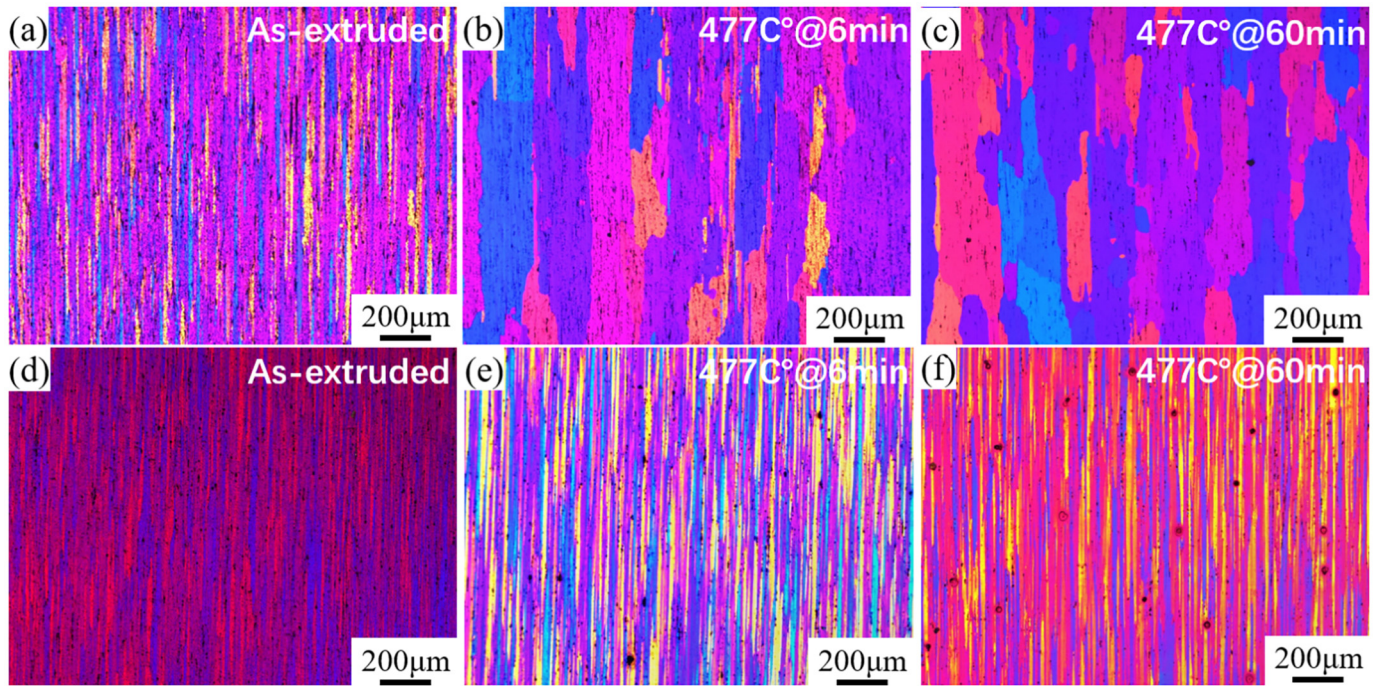
Fig. 8. Polarized light metallographs showing microstructure evolution samples under different states. HH1 sample: (a) as-extruded, (b) 477 °C@6 min, (c) 477 °C@60 min; HH2 sample: (a) as-extruded, (b) 477 °C@6 min, (c) 477 °C@60 min.

coherent with the matrix with a diameter of ~20 nm, which are helpful for improving the pinning effect of dislocations. In comparison, the Al$_3$Zr particles are fewer in HH1 sample (Fig. 10a) than HH2 sample (Fig. 10b). First, precipitation of Al$_3$Zr particles is mainly controlled by diffusion rate of Zr atoms. Secondly, the diffusion distance during annealing at low temperature is ignored because diffusion rate is significantly smaller. Therefore, HH2 sample is annealed at 300 °C@36 h and 470 °C@15 h, the diffusion distance at 300 °C can be ignored. The diffusion rate of Zr in Al matrix at a given temperature is calculated from [5,51,52]:

$$D = D_0 \exp\left(\frac{-Q}{RT}\right) \tag{2}$$

where $D_0 = 7.28 \times 10^{-2}$ m^{2}s^{-1} and $Q = 242$ kJ/mol [25]. The diffusion rates of Zr in Al matrix at the studied temperatures of 300 °C, 400 °C and 470 °C are 6.34×10^{-24}, 1.20×10^{-20} and 7.07×10^{-19} m^{2}s^{-1}, respectively. Thus, diffusion distance L_{dd} in three dimensions can be estimated by [51,52]:

$$L_{dd} = \sqrt{6Dt} \tag{3}$$

where D is diffusion rate at annealing temperature and t is annealing time. Before solution treatment, the duration and temperature of heating are varied. The calculated diffusion distance L_{dd} of HH1 and HH2 samples are 16.1 nm and 478.6 nm, respectively. Therefore, such small diffusion distance of Zr for HH1 sample will be detrimental to precipitation and growth of Al$_3$Zr, leading to lower density of Al$_3$Zr particles.

The GBs/sub-GBs can also be pinned by Al$_3$Zr particles in HH2 sample, and thus increase the resistance to recrystallization (Fig. 10b). Owing to the more Al$_3$Zr particles in HH2 sample, the dislocations are more difficult to move during solution treatment, which can impede the recovery process. Dislocation evolution and Al$_3$Zr particles of two samples during solution treatment are significantly different, as illustrated in Fig. 11. For HH1 sample, some coarse phases remained inside grain before extrusion. After hot

extrusion, a great number of dislocation walls dislocation lines and dislocation tangles formed. During solution treatment, dislocations will rearrange. Few dislocations remained inside grain in as-solutionized HH1 sample (Fig. 11a). For HH2 sample, a high number density of Al$_3$Zr particles formed after pretreatment. After hot extrusion, a great number of dislocation structure formed. In as-solutionized HH2 sample, a large number of dislocations remained because of the pinning effect of Al$_3$Zr particles on dislocations (Fig. 11b).

Evidently, the resistance of recovery and recrystallization in HH2 should be much higher than HH1 sample because the coherent Al$_3$Zr particles are induced in HH2 sample by pretreatment before extrusion, which significantly increase the microstructure stability.

4.2. Strengthening mechanisms

4.2.1. Improved yield strength by pretreatment

In comparison with the HH1 sample, the YS of HH2 sample at T6 state is increased by 171 MPa due to the pretreatment. Owing to the same alloy composition, solution treatment and aging processes for two samples, the difference in strengthening contribution by solution atoms for HH1 and HH2 samples can be ignored. Hence, the enhanced YS of HH2 sample is mainly contributed from: i) Grain refinement strengthening; ii) Precipitation strengthening caused by Al$_3$Zr particles and precipitates; iii) Dislocation strengthening. In addition, the effect of textures on strength is also considered via calculating the average Taylor factor (M) from EBSD date.

i) Grain refinement strengthening.

It is well known that GBs are the main source of yield strength and it can be described by the Hall-Petch relationship [53]. The increased strength caused by grain size can be expressed as [53,54]:

$$\Delta\sigma_d = kd^{-\frac{1}{2}} \tag{4}$$

where d is the average grain size, k is a material-dependent constant that represents the contribution of GB to the related strengthening (0.12 MPa$\sqrt{\text{m}}$ for peak-aged Al-Zn-Mg-Cu alloy [54]). In Eq. (4), the
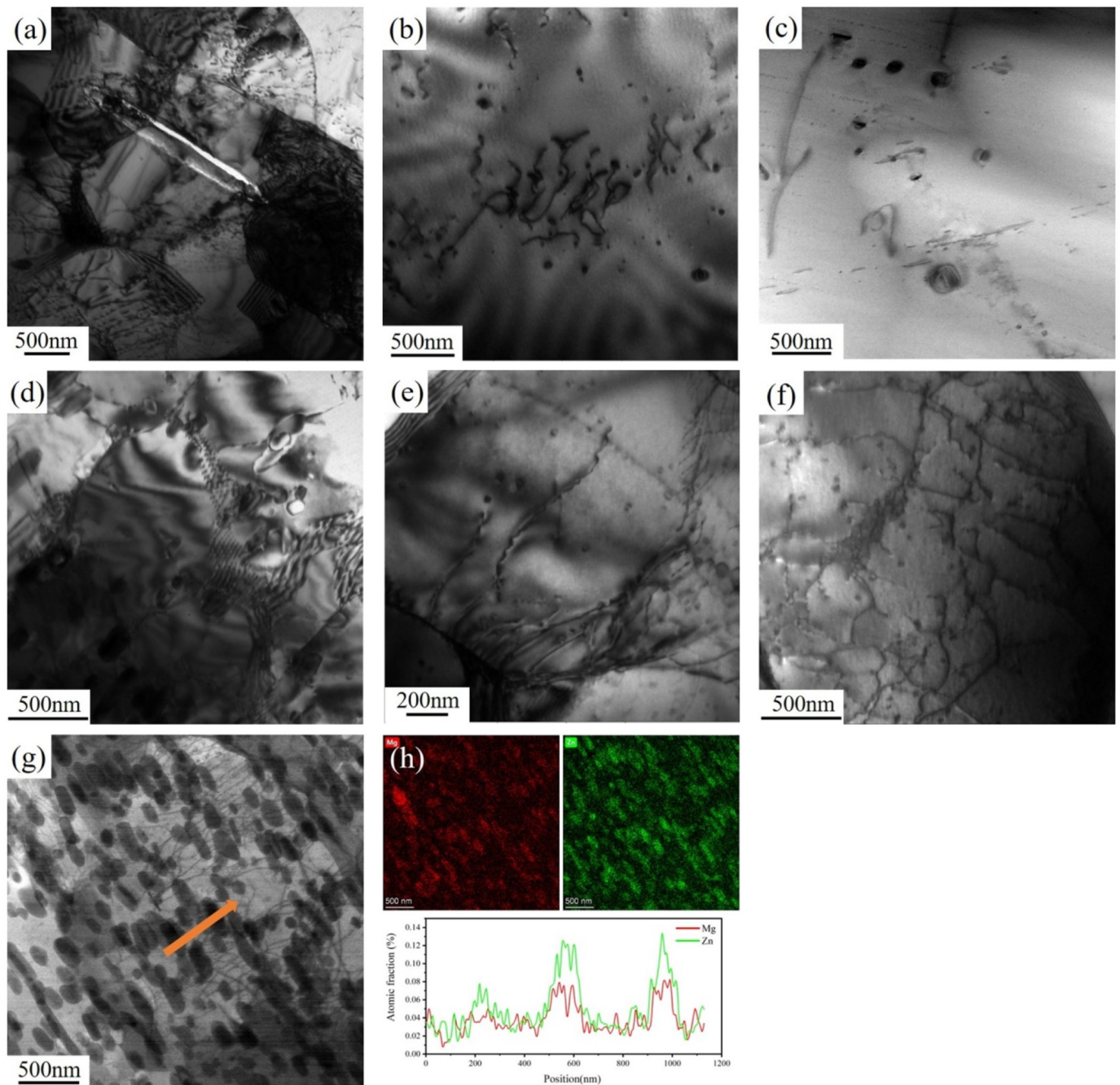
Fig. 9. TEM BF images showing microstructures at different states. HH1 sample: (a) as-extruded, (b) 477 °C@6 min, (c) 477 °C@60 min. HH2 sample: (d) as-extruded, (e) 477 °C@6 min, (f) 477 °C@60 min; (g) STEM BF image of as-extruded HH2, (h) corresponding element mappings and line scanning.

average grain size (d) is evaluated by the cross-sectional IPF maps of the extrusion rods since the cross-sections are normal to the loading stress. As shown in Fig. 4, the d value of HH1-T6 and HH2-T6 sample is 37.4 μm and 6.3 μm, respectively. Thus, $\Delta\sigma_d$ is 19.6 MPa for HH1 and 47.8 MPa for HH2.

ii) Precipitation strengthening caused by Al$_3$Zr particles and precipitates.

In comparison with HH1 sample (Fig. 10a), HH2 sample (Fig. 10b) has a higher number density of Al$_3$Zr particles. The augment of yield strength via Orowan strengthening ($\Delta\sigma_{or}$) mechanism can be analyzed as reported in [55]:

$$\Delta\sigma_{\mathrm{or}} = K \frac{MGb}{\sqrt{1-\nu}} \frac{\ln(d_s/b)}{\lambda} \tag{5}$$

where K is a constant, the value of which depends on the particle size distribution, and d_s and λ are the mean particle diameter and an effective inter-particle distance, respectively, both on the dislocation slip planes, M is average Tylor factor, which is affected by texture, G is the shear modulus (26.9 GPa for Al-Zn-Mg-Cu alloys [51]), b is the magnitude of Burgers vector (0.285 nm), ν is the Poisson's ratio of the Al (0.33). Based on modified particle size distribution, calculated results and experimental results, the precipitation strengthening ($\Delta\sigma_{ppt}$) was
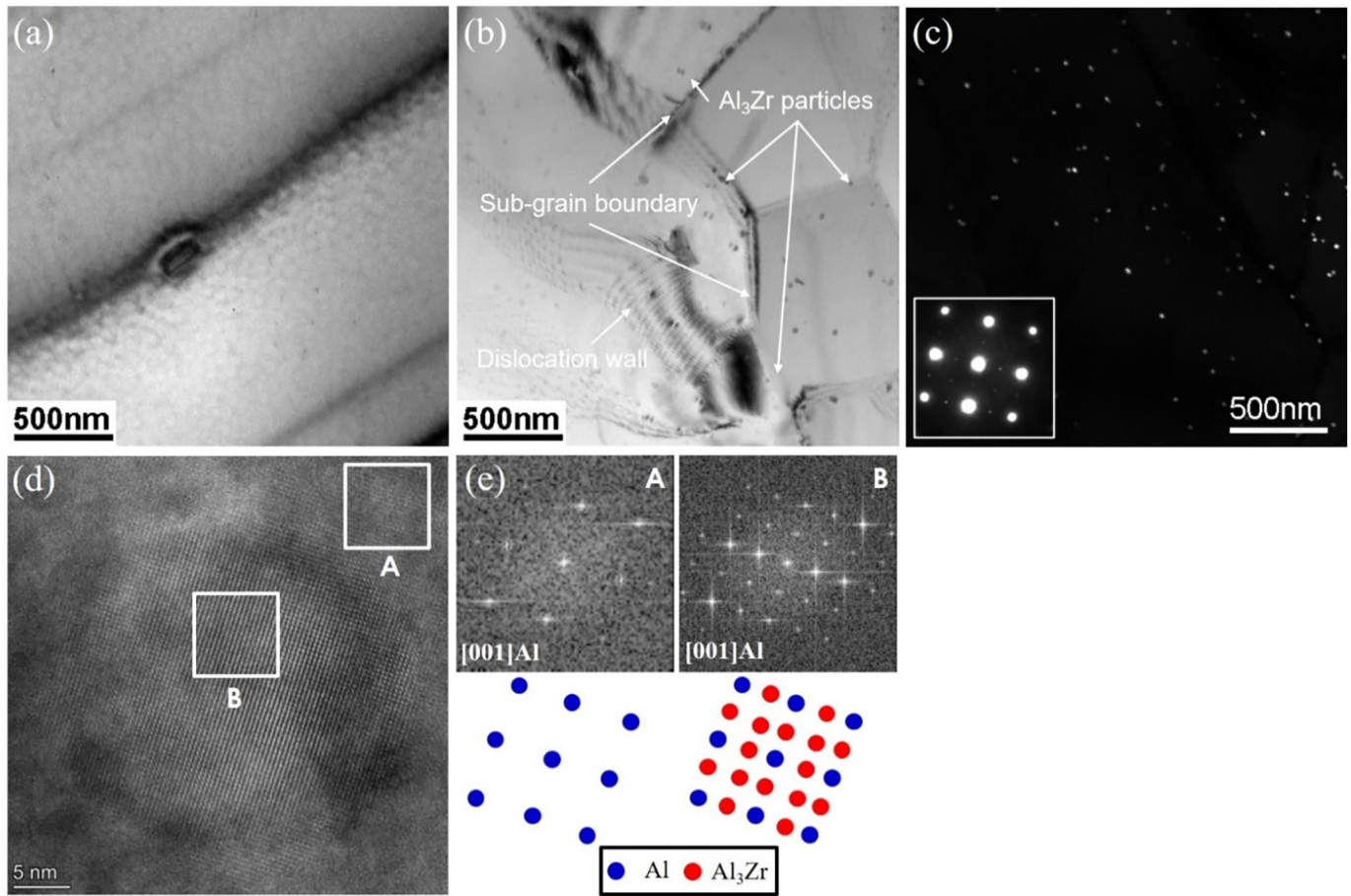
Fig. 10. (a) BF image in as-solutionized HH1 sample (477 °C@60 min), (b) BF image showing Al₃Zr pinning at sub-GB/GB in HH2 sample (c) central dark field image in as-solutionized HH2 sample and inset is corresponding SAED, (d) HRTEM of Al₃Zr (e) the corresponding FFT image of (d).

estimated by applying the following Orowan equations for different precipitates [51,54,55]:

$$\Delta\sigma_{or1} = 13209 \frac{4b}{\pi d_m} \frac{1}{\left[\frac{1}{2}\sqrt{\frac{2\pi}{3f_v}}-1\right]} \ln\left(\frac{\pi d_m}{4b}\right) \tag{6a}$$

$$\Delta\sigma_{or2} = M \frac{0.4Gb}{\pi\sqrt{1-\nu}} \frac{\ln(2\bar{r}/b)}{\lambda_p} \tag{6b}$$

$$f_v = \frac{\pi}{4\left(\frac{\lambda_p}{\bar{r}}+1\right)^2} \tag{6c}$$

where $\Delta\sigma_{or1}$ is developed to estimate the effect of Al₃(Sc,Zr) particles, d_m is the mean particle diameter and f_v is the volume fraction. Therefore, the eq. (6a) suggests that the higher YS value is obtained with larger number density of particles. In this work, the d_m and f_v are 21.53 nm and 0.34% for HH2 sample. In comparison with the HH2 sample, the
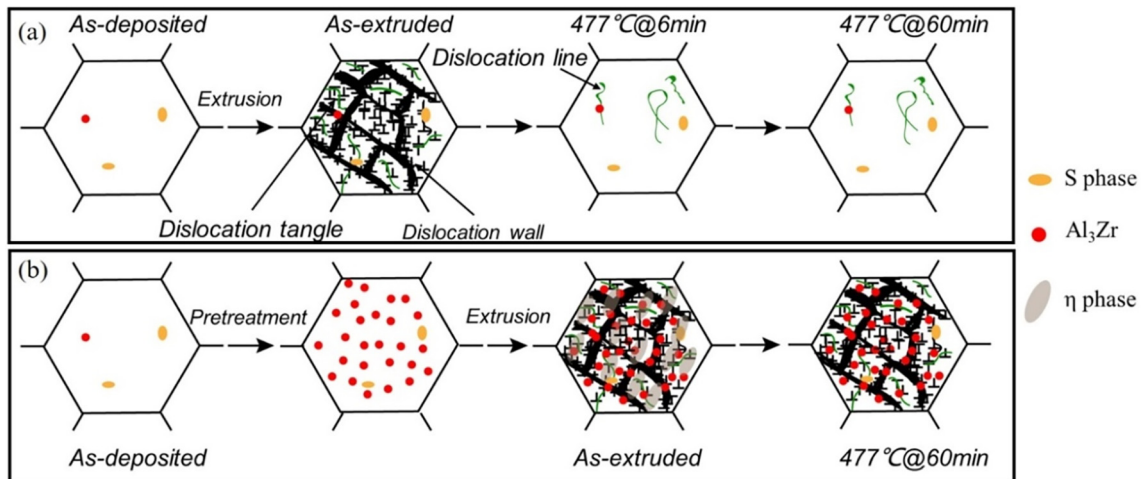
Fig. 11. Schematic showing the dislocation evolutions associated with precipitates during pretreatment, hot-extrusion and solution treatment: (a) HH1 sample, (b) HH2 sample.

number density and fraction volume for HH1 sample are so small that the contribution to strengthen is neglected. The precipitation strengthening caused by Al$_3$Zr particles is 79.9 MPa.

In eq. (6b) and (6c),$\Delta\sigma_{or2}$ is used to describe the contribution of precipitates (GP zones and η' phases), $\bar{r}$ is the mean radius of a circular cross section in a random plane for a spherical precipitate, $\bar{r} = \sqrt{2/3}r$, and r is the mean radius of the precipitates; λ_p is the edge-to-edge inter-precipitate spacing. The precipitate size distribution and $\bar{r}$ is shown in Fig.6g, thus r is 3.25 nm for HH1-T6 and 2.96 nm for HH2-T6. In addition, the mean edge-to-edge inter-precipitate spacing (λ_p) is 38.5 nm and 33.2 nm. Therefore, the precipitation strengthening of HH1-T6 and HH2-T6 is 271.4 MPa and 341.7 MPa, respectively. The smaller precipitates in HH2-T6 sample are mainly attributed to the more uniform dislocations and finer grains (Fig. 2e-f, Fig. 4a-b), which can provide more nucleation sites of precipitates within grains [44,54]. As a result, the precipitation strengthening of HH2-T6 sample is enhanced by pretreatment, i.e., increased by 70.3 MPa in comparison with the HH1-T6 sample.

iii) Dislocation strengthening.

Fig. 9 shows that dislocation density of HH2 sample is higher than that of HH1 sample due to pinning effect of Al$_3$Zr particles. The enhanced dislocation density will cause dislocation strengthening as follow [56]:

$$\Delta\sigma_{dis} = \alpha GbM\sqrt{\rho} \tag{7}$$

where ρ is dislocation density and α is a numerical constant (0.28 in present work). The dislocation density of two samples is different (8.3×10^{12} m^{-2} for HH1-T6 sample and 7.5×10^{13} m^{-2} for HH2-T6 sample). Therefore, the contribution of dislocation to strengthen is 17.9 MPa and 60.5 MPa, respectively.

Consequently, the enhanced strengthen of HH2-T6 sample is mainly contributed by the increased precipitation strengthening of Al$_3$Zr particles and precipitates. Both dislocation strengthening and grain refinement strengthening account for ~32% in the total increment of strength. Comparatively, the strength increment directly caused by lifted dislocation density and refined grain size is much lower.

4.2.2. Influence of pretreatment and aging treatment on the work hardening rate

It is observed that Al$_3$Zr particles are induced by pretreatment and the GP zones, η' phases are induced by aging treatment. In this section, the effect of pretreatment and aging treatment on the work hardening rate (WHR) is discussed. True stress and true plastic strain behavior of metals and alloys are described by Voce strain hardening law as [57,58]:

$$\sigma = \sigma_S - (\sigma_S - \sigma_I)\exp\left[\frac{\varepsilon - \varepsilon_I}{-\epsilon_{tr}}\right] \tag{8}$$

where σ_S is the saturation stress, σ_I and ε_I are the true stress and true plastic strain for constant strain rate, respectively, and ε_{tr} is a characteristic transient strain, a parameter indicating the rate at which the stress σ approaches its saturation values σ_S. The Taylor equation is the basis of all the constitutive equation to describe the true stress-strain curve after plastic deformation which links the total dislocation density as [58]:

$$\hat{\sigma} = M\alpha Gb\sqrt{\rho} \tag{9}$$

Kocks and Mecking present a phenomenological approach to macroscopic plasticity of metals that appears very useful in describing plastic flow under different deformations [57,58]. In Kocks-Mecking model (K-M model), the change in dislocation density may be considered to consist of two components [59]:

$$\frac{d\rho}{d\varepsilon} = M(k_1\sqrt{\rho} - k_2\rho) \tag{10}$$

where the $k_1\sqrt{\rho}$ represents the dislocation storage capacity such as multiplication of mobile dislocations, $k_2\rho$ represents the dislocation recovery including cross-slip mechanism at low temperature and dislocation climb at elevated temperature.

By combining eq. (8) and definition of WHR, the plastic stress dependency of WHR can be derived in the form of [59]:

$$\theta = \theta_0\left(1 - \frac{\sigma}{\sigma_S}\right) \tag{11a}$$

$$\theta_0 = \frac{1}{2}M^2\alpha Gbk_1 \tag{11b}$$

$$\sigma_S = M\alpha Gb\frac{k_1}{k_2} \tag{11c}$$

where θ_0 is the limit value of strain hardening rate for $\sigma \rightarrow 0$. Fig. 12 shows the relationship between θ and σ in two samples. The intercept of θ axis and slope of two samples are listed in Table. 4. For pure aluminum, the θ-axis intercept is assumed to equal to G/20. In the present work, it is obvious that the initial WHR which is the intercept with θ-axis when plastic stress is zero is higher than pure aluminum and increases with the precipitation of Al$_3$Zr. Both k_1 and k_2 value of as-solutionized HH2 sample are larger than that of as-solutionized HH1 sample. The increasing storage rate and recovery rate are related to the non-shearable Al$_3$Zr particles, which can cause dislocation loops and these loops may rearrange through various relaxation mechanisms as deformation proceeds, leading to an increased global storage rate for dislocations [60,61].

The modified KM model took the additional storage of geometrically necessary dislocations into consideration and can be expressed as [62]:

$$\frac{d\rho}{d\varepsilon} = M\left(k_1\sqrt{\rho} - k_2\rho + \frac{1}{bL}\right) \tag{12}$$

The additional dislocation storage due to Al$_3$Zr particles and precipitates is inverse proportional to particle spacing L. In consideration of the additional dislocations annihilation in pairs due to the introduction of particles, the rate of dislocation dynamic recovery can be described by k_2 [63]:

$$k_2 = k_2^0\exp\left(-\frac{L_0}{L}\right) + k_2^p\left[1 - \exp\left(-\frac{L_0}{L}\right)\right] \tag{13}$$

where the first term represents the rate of dislocation recovery without particles, the second term shows the rate of dislocation recovery with particles, L_0 is the mean moving dislocation distance. And $k_2^p \gg k_2^0$, so the k_2 increases with the decrease in particle spacing. Therefore, the particle spacing is decreased by the pretreatment due to more Al$_3$Zr particles induced, thus the dislocation recovery should be promoted.

After aging treatment, the dependence of the WHR on the plastic stress is shown in Fig. 12b. The initial WHR increases with precipitates. Compared with the as-solutionized samples, both k_1 and k_2 are enhanced by aging treatment in two samples. However, the increment of k_1 and k_2 for HH1 sample is 105% and 342% and for HH2 sample is 34% and 188%, respectively. The increment of k_2 is much larger than k_1, which are related to the coherency of GP zones and η' phases. The coherent match affects the dislocation storage slightly while playing an important role in improving dislocation recovery [63,64]. In general, the aging treatment affect work hardening rate mainly by enhancing dislocation recovery rate.
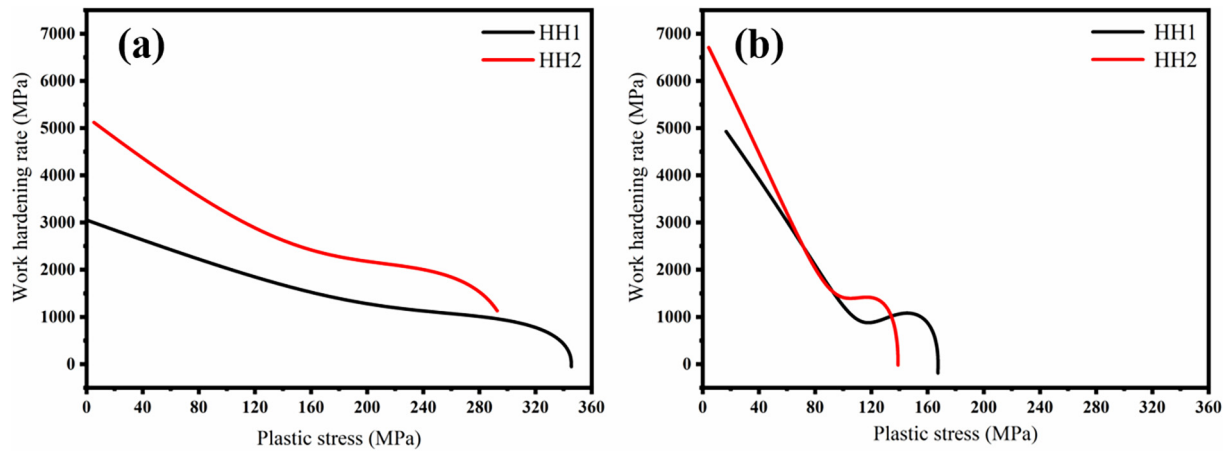
Fig. 12. Plastic stress ($\sigma - \sigma_y$) dependence of the work hardening rate of both HH1 and HH2 samples (a) as-solutionized state (477 °C@60 min), (b) T6 state.

Table 4
Calculating results of Kocks-Mecking model in present work.

State	Sample	θ_0 (MPa)	σ_S (MPa)	k	k_1 (10^8)	k_2
As-solutionized	HH1	2739	269.3	−10.17	3.03	7.01
	HH2	5121	237.1	−21.60	4.51	13.28
T6	HH1	5605	124.8	−44.91	6.21	30.96
	HH2	6884	110.6	−62.22	6.06	38.27

4.2.3. Fracture surface and mechanism of two samples

Fig. 13 shows the tensile fracture surfaces of SF 7050 Al alloys after T6 treatment. Fine dimples are found in both HH1-T6 and HH2-T6 samples, indicating typical ductile fracture features. However, the difference in fracture features can be observed in two samples. In comparison, the fracture surface of HH1-sample is much smooth compared to HH2-T6 sample. Importantly, dimples in the fracture surface of HH1 sample are more than the HH2 one (Fig. 13a and c). The dimple size in
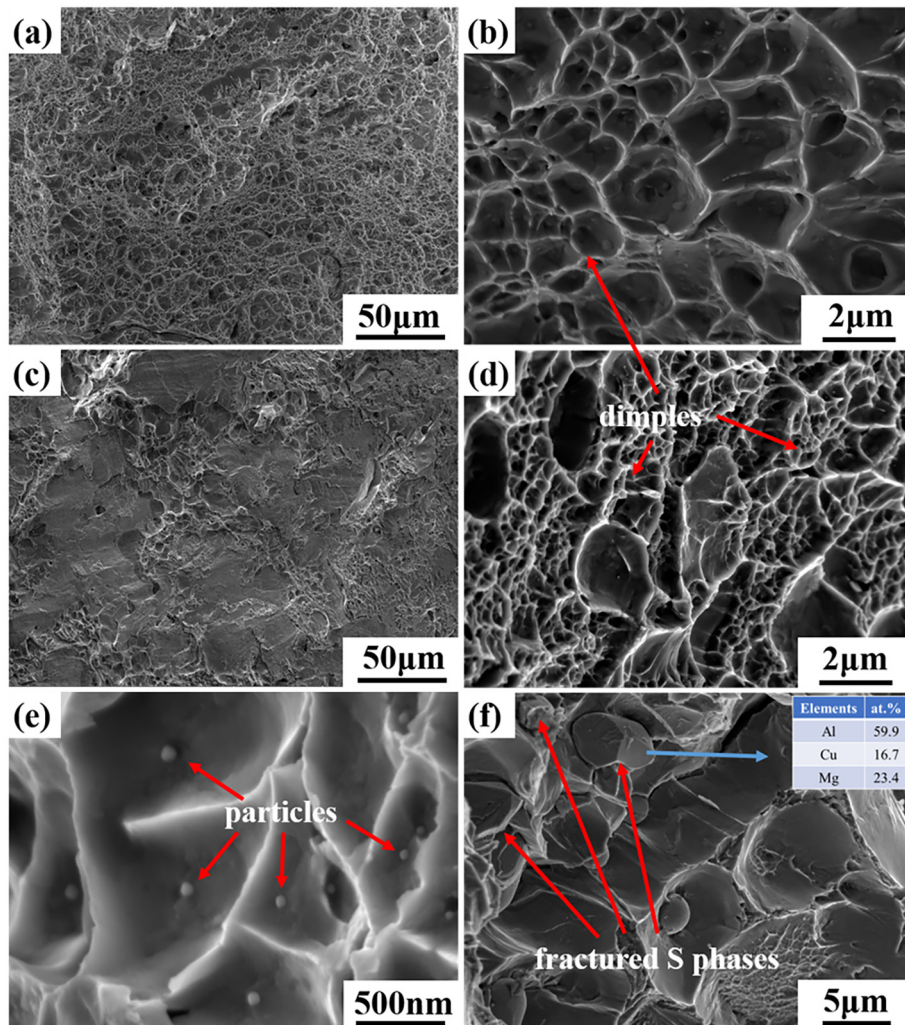

Fig. 13. SEM images showing the tensile fractures of the SF 7050 Al alloy: (a) and (b) HH1-T6; (c), (d), (e) and (f) HH2-T6.

HH2-T6 sample is smaller than HH1-T6 sample, which should be related to more Al$_3$Zr particles distributed in HH1-T6 sample (Fig. 10b and c). The dispersed Al$_3$Zr particles can promote the deformation more homogeneous and enhance strengthen. With the dislocations pinning-up around Al$_3$Zr particles, the stress is lifted at the interfaces of the particles, leading to the formation and growth of voids around hard particles. As shown in Fig. 13e, the dimples with embedded Al$_3$Zr particles can be apparently found. In addition, partial AlZnMgCu phases in 7050 Al alloy can be transformed into S(Al$_2$CuMg) phases during heat treatment and the S phases are hard to be completely dissolved at solution temperature [65,66]. For the HH2 sample, S phases are detected after pretreatment, while they are rarely found in sample HH1 without pretreatment (Fig. 2b). In this case, the localized brittle fracture caused by the coarse S phases occurs in HH2-T6 sample (Fig. 13f), which may accelerate the damage during plastic deformation. Therefore, the ductility of HH2-T6 sample is much lower than HH1-T6 sample, in accordance with the results of tensile curve and work hardening behavior.

5. Conclusions

The 7050 Al alloy billets were fabricated by spray forming (SF) method. It is found that the grain coarsening occurred during the following solution treatment when the billet was processed by the conventional route for SF alloy. A pretreatment before hot extrusion was proposed for the SF 7050 Al alloy. The correlative effects on microstructural stability during solution treatment and the mechanical properties were investigated. The strengthening mechanisms correlated with the microstructure evolution were discussed. The main conclusions are summarized as follows:

(1) Both the as-extruded SF 7050 Al alloy with and without pretreatment, the microstructure features are similar, showing <001> + ⟨111⟩ fiber textures along extrusion direction. The average grain size of HH1 and HH2 sample is 8.9 μm and 11.4 μm, respectively. Both two samples show the comparative grain size.

(2) For the SF 7050 Al alloy directly extruded from the SF billet (conventional process), the grain growth phenomenon dramatically occurs in the following solution treatment due to recrystallization, showing the worse microstructural stability in SF 7050 Al alloy.

(3) For the SF 7050 Al alloy extruded after treated with a pretreatment process, the microstructural stability in the following solution treatment is greatly enhanced. The improvement of microstructural stability is attributed to a large number of dispersed Al$_3$Zr particles introduced by the pretreatment before extrusion, which can pin dislocations, GBs and sub-GBs. In addition, the precipitation during artificial aging is indirectly optimized by the pretreatment.

(4) The work hardening behavior of SF 7050 Al alloy can be significantly affected by the pretreatment and aging treatment. The influence of pretreatment on work hardening rate (WHR) is accomplished by Al$_3$Zr particles. The effect of aging treatment on WHR is caused by precipitation of precipitates, which enhance the dislocation recovery rate.

(5) The strength of SF 7050 Al alloy can be enhanced significantly by this pretreatment approach. The yield strength and ultimate strength are enhanced from 512 MPa and 602 MPa to 683 MPa and 745 MPa, respectively. The enhancement of strength is mainly related to the induced Al$_3$Zr particles and the optimized precipitates by the pretreatment.

Declaration of Competing Interest

No potential conflict of interest was reported by the authors.

Acknowledgments

References

[1] Y. Liu, D. Jiang, B. Li, W. Yang, J. Hu, Effect of cooling aging on microstructure and mechanical properties of an Al-Zn-Mg-Cu alloy, Mater. Des. 57 (2014) 79–86.

[2] A. Azarniya, A.K. Taheri, K.K. Taheri, Recent advances in ageing of 7xxx series aluminum alloys: a physical metallurgy perspective, J. Alloys Compd. 781 (2019) 945–983.

[3] T. Dursun, C. Soutis, Recent developments in advanced aircraft aluminium alloys, Mater. Des. 56 (2014) 862–871.

[4] Y. Wang, G. Zhao, X. Xu, X. Chen, W. Zhang, Microstructures and mechanical properties of spray deposited 2195 Al-Cu-Li alloy through thermo-mechanical processing, Mater. Sci. Eng. A 727 (2018) 78–89.

[5] E.J. Lavernia, Y. Wu, Spray Atomization and Deposition, John Wiley, New York, 1996.

[6] M.M. Sharma, M.F. Amateau, T.J. Eden, Mesoscopic structure control of spray formed high strength Al-Zn-Mg-Cu alloys, Acta Mater. 53 (2005) 2919–2924.

[7] W.D. Cai, J. Smugeresky, E.J. Lavernia, Low-pressure spray forming of 2024 aluminum alloy, Mater. Sci. Eng. A 241 (1998) 60–71.

[8] Y. Jia, F. Cao, S. Guo, P. Ma, J. Liu, J. Sun, Hot deformation behavior of spray-deposited Al-Zn-Mg-Cu alloy, Mater. Des. 53 (2014) 79–85.

[9] R. Su, J. Su, Y. Qu, J. You, R. Li, Retrogression on corrosion behavior of spray formed Al-7075, J. Mater. Res. 32 (2017) 2621–2627.

[10] L.L. Liu, Q.L. Pan, X.D. Wang, S.W. Xiong, The effects of aging treatments on mechanical property and corrosion behavior of spray formed 7055 aluminium alloy, J. Alloys Compd. 735 (2018) 261–276.

[11] E.M. Mazzer, C.R.M. Afonso, C. Bolfarini, C.S. Kiminami, Microstructure study of Al 7050 alloy reprocessed by spray forming and hot-extrusion and aged at 121°C, Intermetallics 43 (2013) 182–187.

[12] E.M. Mazzer, C.R.M. Afonso, M. Galano, C.S. Kiminami, C. Bolfarini, Microstructure evolution and mechanical properties of Al-Zn-Mg-Cu alloy reprocessed by spray-forming and heat treated at peak aged condition, J. Alloys Compd. 579 (2013) 169–173.

[13] H.A. Godinho, A.L.R. Beletati, E.J. Giordano, C. Bolfarini, Microstructure and mechanical properties of a spray formed and extruded AA7050 recycled alloy, J. Alloys Compd. 586 (2014) S139–S142.

[14] J.M. Schreiber, Z.R. Omcikus, T.J. Eden, M.M. Sharma, V. Champagne, S.N. Patankar, Combined effect of hot extrusion and heat treatment on the mechanical behavior of 7055 AA processed via spray metal forming, J. Alloys Compd. 617 (2014) 135–139.

[15] Y. Jia, F. Cao, Z. Ning, S. Guo, P. Ma, J. Sun, Influence of second phases on mechanical properties of spray-deposited Al-Zn-Mg-Cu alloy, Mater. Des. 40 (2012) 536–540.

[16] H. Yu, M. Wang, X. Sheng, Z. Li, L. Chen, Q. Lei, C. Chen, Y. Jia, Z. Xiao, W. Chen, H. Wei, H. Zhang, X. Fan, Y. Wang, Microstructure and tensile properties of large-size 7055 aluminum billets fabricated by spray forming rapid solidification technology, J. Alloys Compd. 578 (2013) 208–214.

[17] B. Liu, Q. Lei, L. Xie, M. Wang, Z. Li, Microstructure and mechanical properties of high product of strength and elongation Al-Zn-Mg-Cu-Zr alloys fabricated by spray deposition, Mater. Des. 96 (2016) 217–223.

[18] X. Zhou, X.Y. Li, K. Lu, Enhanced thermal stability of nanograined metals below a critical grain size, Science 360 (2018) 526–530.

[19] A.M. Cassell, J.D. Robson, C.P. Race, A. Eggeman, T. Hashimoto, M. Besel, Dispersoid composition in zirconium containing Al-Zn-Mg-Cu (AA7010) aluminium alloy, Acta Mater. 169 (2019) 135–146.

[20] Y. Deng, Y. Zhang, L. Wan, A.A. Zhu, X. Zhang, Three-stage homogenization of Al-Zn-Mg-Cu alloys containing trace Zr, Metall. Mater. Trans. A 44 (2013) 2470–2477.

[21] Z. Guo, G. Zhao, X.G. Chen, Effects of two-step homogenization on precipitation behavior of Al$_3$Zr dispersoids and recrystallization resistance in 7150 aluminum alloy, Mater. Charact. 102 (2015) 122–130.

[22] J.L. Ning, D.M. Jiang, Influence of Zr addition on the microstructure evolution and thermal stability of Al-Mg-Mn alloy processed by ECAP at elevated temperature, Mater. Sci. Eng. A 452-453 (2007) 552–557.

[23] E. Clouet, J.M. Sanchez, C. Sigli, First-principles study of the solubility of Zr in Al, Phys. Rev. B 65 (2002).

[24] L.M. Wu, W.H. Wang, Y.F. Hsu, S. Trong, Effects of homogenization treatment on recrystallization behavior and dispersoid distribution in an Al-Zn-Mg-Sc-Zr alloy, J. Alloys Compd. 456 (2008) 163–169.

[25] J.D. Robson, P.B. Prangnell, Dispersoid precipitation and process modelling in zirconium containing commercial aluminium alloys, Acta Mater. 49 (2001) 599–613.

[26] A. Ditta, L. Wei, Y. Xu, S. Wu, Effect of hot extrusion and optimal solution treatment on microstructure and properties of spray-formed Al-11.3Zn-2.65Mg-1Cu alloy, J. Alloys Compd. 797 (2019) 558–565.

[27] L. Li, L. Wei, Y. Xu, L. Mao, S. Wu, Study on the optimizing mechanisms of superior comprehensive properties of a hot spray formed Al-Zn-Mg-Cu alloy, Mater. Sci. Eng. A 742 (2019) 102–108.

[28] S.L. Dai, J.P. Delplanque, E.J. Lavernia, Grain growth in reactive spray deposited 5083 alloys, Scr. Mater. 40 (1998) 145–151.

[29] L. Xie, Q. Lei, M. Wang, X. Sheng, Z. Li, Effects of aging mechanisms on the exfoliation corrosion behavior of a spray deposited Al–Zn–Mg–Cu–Zr aluminum alloy, J. Mater. Res. 32 (2017) 1105–1117.

[30] X. Wang, Q. Pan, L. Liu, S. Xiong, W. Wang, J. Lai, Y. Sun, Z. Huang, Characterization of hot extrusion and heat treatment on mechanical properties in a spray formed ultra-high strength Al-Zn-Mg-Cu alloy, Mater. Charact. 144 (2018) 131–140.

[31] ASTM E8/E8M-15a, Standard Test Methods for Tension Testing of Metallic Materials, 2015.

[32] F. Jiang, H. Zhang, J. Su, Y. Sun, Constitutive characteristics and microstructure evolution of 7150 aluminum alloy during isothermal and non-isothermal multistage hot compression, Mater. Sci. Eng. A 636 (2015) 459–469.

[33] F. Xie, X. Yan, L. Ding, F. Zhang, S. Chen, M.G. Chu, Y.A. Chang, A study of microstructure and microsegregation of aluminum 7050 alloy, Mater. Sci. Eng. A 355 (2003) 144–153.

[34] Z. Xie, Z. Jia, K. Xiang, Y. Kong, Z. Li, X. Fan, W. Ma, H. Zhang, L. Lin, K. Marthinsen, Q. Liu, Microstructure evolution and recrystallization resistance of a 7055 alloy fabricated by spray forming technology and by conventional ingot metallurgy, Metall. Mater. Trans. A 51 (2020) 5378–5388.

[35] G.K. Williamson, W.H. Hall, X-ray line broadening from filed aluminium and wolfram, Acta Metall. 1 (1953) 22–31.

[36] G.K. Williamson, R.E. Smallman III, Dislocation densities in some annealed and cold-worked metals from measurements on the X-ray debye-scherrer spectrum, Philos. Mag. 1 (1956) 34–46.

[37] T.F. Chung, Y.L. Yang, M. Shiojiri, C.N. Hsiao, W.C. Li, C.S. Tsao, Z. Shi, J. Lin, J.R. Yang, An atomic scale structural investigation of nanometre-sized η precipitates in the 7050 aluminium alloy, Acta Mater. 174 (2019) 351–368.

[38] K.M. McHugh, J.P. Delplanque, S.B. Johnson, E.J. Lavernia, Y. Zhou, Y. Lin, Spray rolling aluminum alloy strip, Mater. Sci. Eng. A 383 (2004) 96–106.

[39] X. Peng, Y. Li, G. Xu, J. Huang, Z. Yin, Effect of precipitate state on mechanical properties, corrosion behavior, and microstructures of Al-Zn-Mg-Cu alloy, Met. Mater. Int. 24 (2018) 1046–1057.

[40] J.F. Li, N. Birbilis, C.X. Li, Z.Q. Jia, B. Cai, Z.Q. Zheng, Influence of retrogression temperature and time on the mechanical properties and exfoliation corrosion behavior of aluminium alloy AA7150, Mater. Charact. 60 (2009) 1334–1341.

[41] J.C. Lin, H.L. Liao, W.D. Jehng, C.H. Chang, S.L. Lee, Effect of heat treatments on the tensile strength and SCC-resistance of AA7050 in an alkaline saline solution, Corros. Sci. 48 (2006) 3139–3156.

[42] Y. Liu, S. Liang, D. Jiang, Influence of repetitious non-isothermal aging on microstructure and strength of Al-Zn-Mg-Cu alloy, J. Alloys Compd. 689 (2016) 632–640.

[43] X. Peng, Q. Guo, X. Liang, Y. Deng, Y. Gu, G. Xu, Z. Yin, Mechanical properties, corrosion behavior and microstructures of a non-isothermal ageing treated Al-Zn-Mg-Cu alloy, Mater. Sci. Eng. A 688 (2017) 146–154.

[44] X. Peng, Y. Li, X. Liang, Q. Guo, G. Xu, Y. Peng, Z. Yin, Precipitate behavior and mechanical properties of enhanced solution treated Al-Zn-Mg-Cu alloy during non-isothermal ageing, J. Alloys Compd. 735 (2018) 964–974.

[45] S.V. Emani, J. Benedyk, P. Nash, D. Chen, Double aging and thermomechanical heat treatment of AA7075 aluminum alloy extrusions, J. Mater. Sci. 44 (2009) 6384–6391.

[46] J.T. Jiang, Q.J. Tang, L. Yang, K. Zhang, S.J. Yuan, L. Zhen, Non-isothermal ageing of an Al-8Zn-2Mg-2Cu alloy for enhanced properties, J. Mater. Process. Technol. 227 (2016) 110–116.

[47] W. Yang, S. Ji, Q. Zhang, M. Wang, Investigation of mechanical and corrosion properties of an Al-Zn-Mg-Cu alloy under various ageing conditions and interface analysis of η' precipitate, Mater. Des. 85 (2015) 752–761.

[48] S. Chen, K. Chen, G. Peng, L. Jia, P. Dong, Effect of heat treatment on strength, exfoliation corrosion and electrochemical behavior of 7085 aluminum alloy, Mater. Des. 35 (2012) 93–98.

[49] W. Wang, Q. Pan, X. Wang, Y. Sun, L. Long, Z. Huang, Mechanical properties and microstructure evolution of ultra-high strength Al-Mg-Cu alloy processed by room temperature ECAP with post aging, Mater. Sci. Eng. A 731 (2018) 195–208.

[50] I.A. MacAskill, A.D.P. LaDepha, J.H. Milligan, J.J. Fulton, D.P. Bishop, Effects of cold and hot densification on the mechanical properties of a 7XXX series powder metallurgy alloy, Powder Metall. 52 (4) (2013) 304–310.

[51] K. Ma, T. Hu, H. Yang, T. Topping, A. Yousefiani, E.J. Lavernia, J.M. Schoenung, Coupling of dislocations and precipitates: impact on the mechanical behavior of ultrafine grained Al-Zn-Mg alloys, Acta Mater. 103 (2016) 153–164.

[52] H. Mehrer, Diffusion in Solids: Fundamentals, Methods, Materials, Diffusion-Controlled Processes, Springer, Berlin, 2007.

[53] C. Genevois, A. Deschamps, A. Denquin, B. Doisneaucottignies, Quantitative investigation of precipitation and mechanical behaviour for AA2024 friction stir welds, Acta Mater. 53 (2005) 2447–2458.

[54] K. Ma, H. Wen, T. Hu, T.D. Topping, D. Isheim, D.N. Seidman, E.J. Lavernia, J.M. Schoenung, Mechanical behavior and strengthening mechanisms in ultrafine grain precipitation-strengthened aluminum alloy, Acta Mater. 62 (2014) 141–155.

[55] O.N. Senkov, M.R. Shagiev, S.V. Senkova, D.B. Miracle, Precipitation of Al₃(Sc,Zr) particles in an Al-Zn-Mg-Cu-Sc-Zr alloy during conventional solution heat treatment and its effect on tensile properties, Acta Mater. 56 (2008) 3723–3738.

[56] M. Zha, Y. Li, R.H. Mathiesen, R. Bjørge, H.J. Roven, Microstructure evolution and mechanical behavior of a binary Al-7Mg alloy processed by equal-channel angular pressing, Acta Mater. 84 (2015) 42–54.

[57] Y. Estrin, Dislocation-density–related constitutive modeling - sciencedirect, Unified Constitutive Laws of Plastic Deformation, 1996 69–106.

[58] U.F. Kocks, Laws for work-hardening and low-temperature creep, J. Eng. Mater. Technol. 98 (1976) 76–85.

[59] Y. Estrin, H. Braasch, Y. Brechet, A dislocation density based constitutive model for cyclic deformation, J. Eng. Mater. Technol. 118 (1996) 441–447.

[60] L.M. Cheng, W.J. Poole, J.D. Embury, D.J. Lloyd, The influence of precipitation on the work-hardening behavior of the aluminum alloys AA6111 and AA7030, Metall. Mater. Trans. A 34 (2003) 2473–2481.

[61] F. Fazeli, W.J. Poole, C.W. Sinclair, Modeling the effect of Al₃Sc precipitates on the yield stress and work hardening of an Al-Mg-Sc alloy, Acta Mater. 56 (2008) 1909–1918.

[62] A. Simar, Y. Brechet, B. de Meester, A. Denquin, T. Pardoen, Sequential modeling of local precipitation, strength and strain hardening in friction stir welds of aluminum alloy 6005A-T6, Acta Mater. 55 (2007) 6133–6143.

[63] Y. Estrin, H. Mecking, A unified phenomenological description of work hardening and creep based on one-parameter models, Acta Metall. 32 (1984) 57–70.

[64] H.T. Jeong, W.J. Kim, Strain hardening behavior and strengthening mechanism in Mg-rich Al-Mg binary alloys subjected to aging treatment, Mater. Sci. Eng. A 794 (2020) 139862.

[65] G. Liu, J.W. Geng, Y.G. Li, L. Cai, D. Chen, M.L. Wang, N.H. Ma, H.W. Wang, Microstructures evolution of nano TiB₂/7050Al composite during homogenization, Mater. Charact. 159 (2020) 110019.

[66] L.G. Hou, W.L. Xiao, H. Su, C.M. Wu, D.G. Eskin, L. Katgerman, L.Z. Zhuang, J.S. Zhang, Room-temperature low-cycle fatigue and fracture behaviour of asymmetrically rolled high-strength 7050 aluminium alloy plates, Int. J. Fatigue 142 (2021) 105919.